Article

Constrained catecholamines gain β₂AR selectivity through allosteric effects on pocket dynamics

Check for updates

Xinyu Xu[1,2], Jeremy Shonberg[3], Jonas Kaindl[3], Mary J. Clark [4], Anne Stößel[3], Luis Maul [3], Daniel Mayer[4], Harald Hübner [3], Kunio Hirata [5,6], A. J. Venkatakrishnan[7,8,9,10], Ron O. Dror [7,8,9,10], Brian K. Kobilka [8] ✉, Roger K. Sunahara [4] ✉, Xiangyu Liu [1,2,11] ✉ & Peter Gmeiner [3] ✉

G protein-coupled receptors (GPCRs) within the same subfamily often share high homology in their orthosteric pocket and therefore pose challenges to drug development. The amino acids that form the orthosteric binding pocket for epinephrine and norepinephrine in the β₁ and β₂ adrenergic receptors (β₁AR and β₂AR) are identical. Here, to examine the effect of conformational restriction on ligand binding kinetics, we synthesized a constrained form of epinephrine. Surprisingly, the constrained epinephrine exhibits over 100-fold selectivity for the β₂AR over the β₁AR. We provide evidence that the selectivity may be due to reduced ligand flexibility that enhances the association rate for the β₂AR, as well as a less stable binding pocket for constrained epinephrine in the β₁AR. The differences in the amino acid sequence of the extracellular vestibule of the β₁AR allosterically alter the shape and stability of the binding pocket, resulting in a marked difference in affinity compared to the β₂AR. These studies suggest that for receptors containing identical binding pocket residues, the binding selectivity may be influenced in an allosteric manner by surrounding residues, like those of the extracellular loops (ECLs) that form the vestibule. Exploiting these allosteric influences may facilitate the development of more subtype-selective ligands for GPCRs.

G protein-coupled receptors (GPCRs) are of great interest as therapeutic targets[1]. One of the major challenges in drug discovery efforts is to minimize off-target side effects, and to achieve greater subtype selectivity of candidate drugs[2]. Many pharmaceutically important GPCRs have multiple closely related subtypes that fulfill different physiologic roles, but are all activated by the same hormone or neurotransmitter. For example, the nine adrenergic receptor subtypes have different roles in regulating central and sympathetic nervous system functions, but can all be activated by epinephrine (Epi) and norepinephrine (NorEpi), as they share a highly homologous orthosteric binding pocket.

The β₁ and β₂ adrenergic receptors (ARs) have been among the most extensively studied G protein-coupled receptors (GPCRs) due to their roles in the regulation of cardiac and pulmonary function by the autonomic nervous system. βAR antagonists were among the first GPCR drugs to be developed and β₁AR-selective antagonists are used for the treatment of heart failure, arrhythmias, and hypertension[3]. β₂AR-selective agonists have been used in the treatment of asthma and chronic obstructive pulmonary disease[4]. β₁AR and β₂AR are equally responsive to Epi, primarily secreted by the adrenal gland, in contrast to NorEpi, which is primarily released from sympathetic nerve terminals, and is approximately 10-fold more selective for the β₁AR[5].

Previous molecular dynamics (MD) simulations of alprenolol and other ligands binding to the β2AR[6] reveal that ligands typically access the orthosteric binding pocket through a portal formed by a narrow cleft, lined by residues in the extracellular vestibule. Recent studies suggest that the preferred pathway may differ for the β1AR and β2AR[7] (Fig. 1a). MD simulations suggest that ligand flexibility might be important for navigating through the extracellular vestibule. Ligand flexibility, however, also yields an entropic penalty when the ligand arrives at the orthosteric pocket, where it is constrained to a single or limited set of conformations. The principle sites of flexibility in catecholamines are contributed by two rotatable bonds, one between the catechol ring and the ethanolamine moiety and one within the ethanolamine itself (see Fig. 1b). A key finding revealed in structural studies of Epi-, NorEpi- and isoproterenol (ISO)-bound β-ARs is the selection of one specific set of rotamers of the catecholamines[8,9].

In this work, to examine the effect of ligand flexibility and the entropic contribution to catecholamine binding to β1AR and β2AR, we generated conformationally-constrained forms of Epi, NorEpi, and ISO to restrict or constrain the rotatable bonds and characterized their pharmacology and signaling behavior. We show that the constrained catecholamines gain β2AR selectivity over the β1AR despite the orthosteric ligand binding sites are identical in these two receptors. We further show that allosteric effects from surrounding residues of the orthosteric pockets alter the shape of the pockets and contribute to the β2AR selectivity of the constrained catecholamines.

Results

Design and characterization of constrained catecholamines

Two bridging carbons were introduced to constrain the conformation of the catecholamines. Because there are two possible ways to rigidify the compound and each constrained compound has two chiral carbons, each catecholamine will have eight possible constrained isomers (Fig. 1c). Compounds 1–4 would not be expected to fit into the previously reported Epi and NorEpi binding pose; nevertheless, we

decided to synthesize and test them for completeness (Supplementary Notes). The synthesis of a subset of similar compounds has previously been described; however, these compounds were not enantiomerically pure, and their pharmacology was not fully characterized[10]. We synthesized all the eight possible isomers of ISO (Supplementary Notes). Of which, the (R,R) form (compound 8, c-ISO) showed the highest affinity for both the β1AR and the β2AR, but not the αARs, in radioligand competition binding assay (Fig. 1d and Supplementary Table 1). Interestingly, the (R,R)-isomer also showed selectivity towards the β2AR over β1AR (Fig. 1e and Supplementary Table 2). Consequently, we synthesized the constrained (R,R)-isomers of Epi and NorEpi (hereby named c-Epi or c-NorEpi) (Supplementary Notes) and characterized their pharmacological properties side-by-side with the non-constrained forms. Compared to Epi, which has a similar EC50 in G protein activation, adenylyl cyclase activation, and arrestin recruitment for both the β1AR and the β2AR, c-Epi exhibited both an increase in potency at the β2AR and a decrease at the β1AR. On the β2AR, c-Epi has a threefold lower EC50 for G protein activation and adenylyl cyclase stimulation and a 7.5-fold reduction in EC50 in an arrestin recruitment assay, compared to the non-rigidified native hormone (Fig. 2a, Supplementary Fig. 1, Supplementary Tables 2, 3). In striking contrast, c-Epi at the β1AR yields a ~14-fold increase in the EC50 in cyclase stimulation and a ~19-fold increase in the EC50 in arrestin recruitment. Radioligand competition binding assays indicate that constrained Epi bound eightfold better on the β2AR but 34-fold worse on the β1AR, compared to unconstrained Epi (Fig. 1e and Supplementary Table 4). Thus, while Epi does not display a preference for either β1AR or β2AR in an arrestin recruitment or radioligand binding assays, c-Epi recruits β-arrestin with an ~600-fold selectivity for β2AR over β1AR. We also note a substantial reduction (~40%) in the Emax for c-Epi-induced arrestin recruitment to β1AR (Fig. 2a and Supplementary Table 3).

Perhaps more interesting is the complete switch in β1AR-β2AR selectivity of NorEpi upon constraining the catecholamine. In β-arrestin recruitment assays NorEpi has ~16-fold selectivity for β1AR
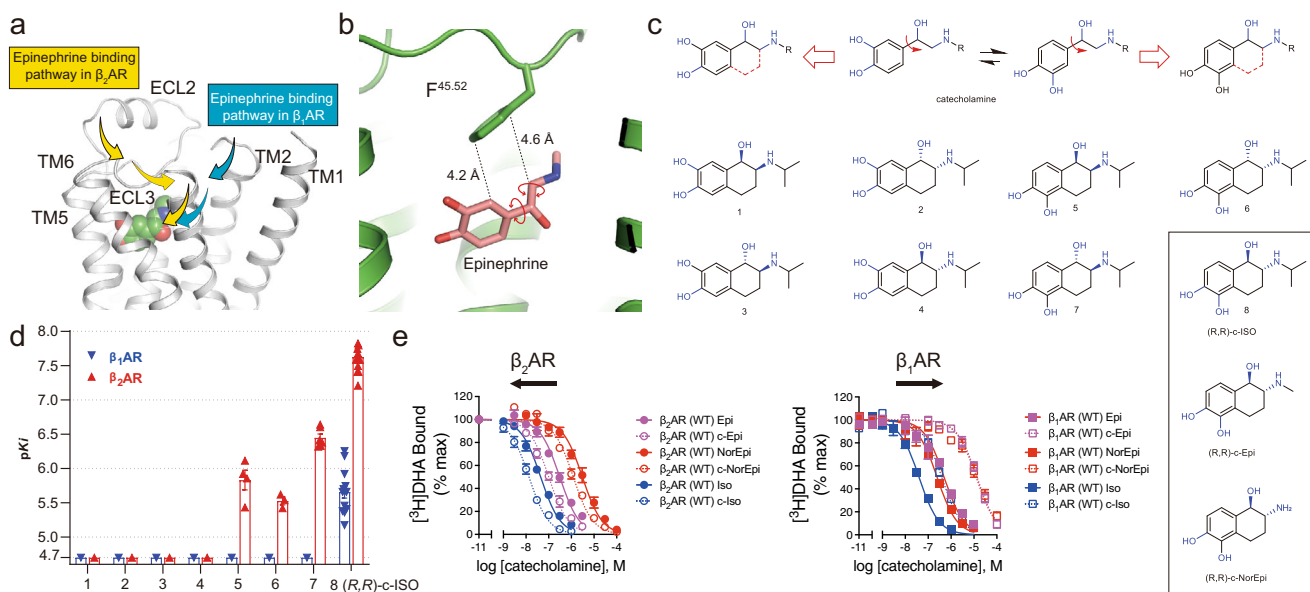

Fig. 1 | Design and synthesis of conformationally-constrained catecholamine. a Epi favors different binding pathways to enter the orthosteric pockets in the β1AR and β2AR[7]. **b** There is space between Epi and F[45.52] to allow the receptor to accommodate for the conformational restriction of the catecholamine (PDB: 4LDO). **c** The design and synthesis flow of eight possible conformationally-constrained isoprenaline isomers and the chemical structures of (R,R)-c-Epi and (R,R)-c-NorEpi. **d** The (R,R)-isomer of c-ISO showed the highest affinity to both the β1AR and β2AR among all the eight possible isomers. Data were given as mean ±

SEM of n = 3 (for **1-4,6**), n = 4 (for **5**), n = 5 (β1AR for **7**), n = 6 (β2AR for **7**), n = 13 (β2AR for **8**), and n = 14 (β1AR for **8**) independent experiments. **e** c-ISO, c-Epi, and c-NorEpi showed β2AR selectivity in a radioligand competition binding assay. Data were given as mean ± SEM of n = 3 (β1AR for Epi), n = 3 (β2AR for Epi), n = 3 (β1AR for NorEpi), n = 5 (β2AR for NorEpi), n = 3 (β1AR for ISO), n = 3 (β2AR for ISO), n = 6 (β1AR for c-Epi), n = 6 (β2AR for c-Epi), n = 5 (β1AR for c-NorEpi), n = 5 (β2AR for c-NorEpi), n = 3 (β1AR for cISO), n = 3 (β2AR for cISO) independent experiments. Source data are provided as a Source Data file.

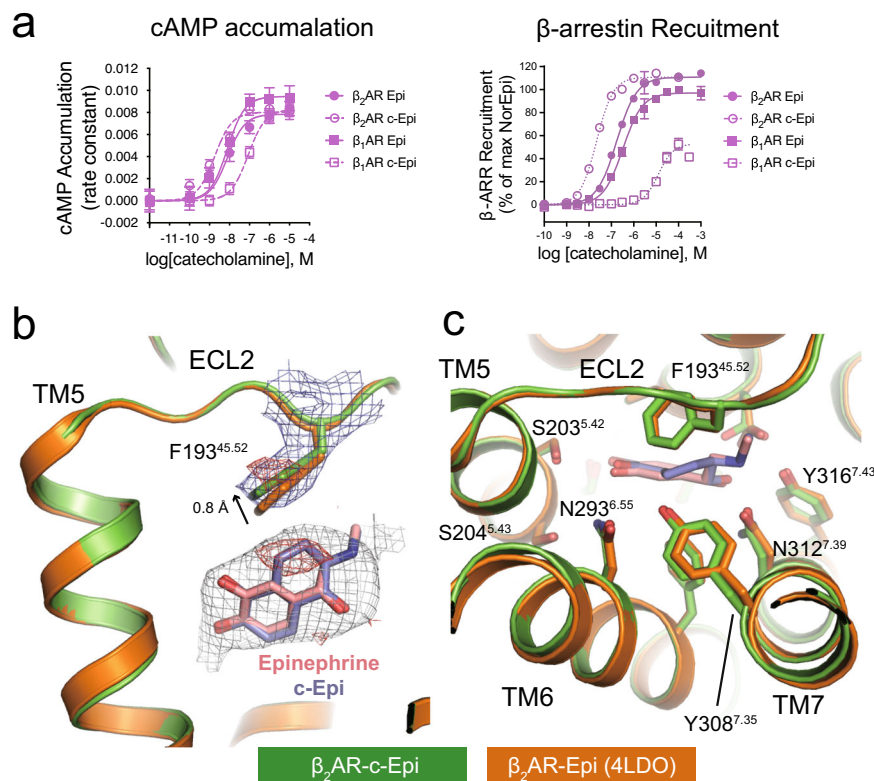**Fig. 2 | c-Epi is selective towards the β_2AR and binds to the same position as Epi does. a** c-Epi shows β_2AR selectivity in both cAMP recruitment and arrestin signaling assays. Data were given as mean ± SEM of $n = 6$ (β_1AR for Epi, arrestin), $n = 15$ (β_1AR for c-Epi, arrestin), $n = 17$ (β_2AR for Epi, arrestin), and $n = 21$ (β_2AR for c-Epi, arrestin) independent experiments. Source data are provided as a Source data file. **b** c-Epi binds in a nearly identical position as Epi in the β_2AR as revealed by the 2fofc density (blue mesh, contoured at 1.0 σ). The extra two carbons of c-Epi compared to Epi as well as the upward movement of F[45.52] are revealed by the isomorphous difference map (red mesh, contoured at 3.0 σ). **c** The binding pocket residues are in similar positions upon Epi or c-Epi binding.

over β_2AR, whereas c-NorEpi displays a 52-fold selectivity for β_2AR over β_1AR (Supplementary Fig. 2 and Supplementary Table 3). For isoproterenol, where the EC$_{50}$ for β_1AR and β_2AR are nearly identical (19 and 16 nM, respectively) and thus, no subtype selectivity. Constrained ISO, however, displays greater than a 70-fold selectivity for β_2AR afforded by a greater than a 100-fold decrease in the potency at β_1AR for recruiting β-arrestin (Supplementary Fig. 2 and Supplementary Table 3). Radioligand binding analysis suggests that this dramatic increase in β_2AR selectivity was contributed by a tenfold decrease in affinity for β_1AR, with a ~3-fold improvement in β_2AR affinity. (Fig. 1e and Supplementary Table 4).

An additional side note is that neither c-NorEpi, c-Epi or c-ISO displayed any appreciable activity for the α_1AR or α_2AR subtypes, suggesting that constraining the catecholamines garners the agonists β_2AR-selective over all adrenergic receptors (Supplementary Fig. 3 and Supplementary Table 2).

Structure determination of the β_2AR–c-Epi complex

What is most striking about the enhanced potency of these constrained catecholamines on β_2AR is the marked decrease in potency at the β_1AR. In an attempt to understand the structural basis for this subtype selectivity, we solved the crystal structures of the β_2AR in complex with c-Epi and c-ISO at 3.2 and 3.4 Å resolution, respectively. The structures were obtained with a previously described nanobody Nb6B9 and a β_2AR construct with T4 lysozyme fused to the N-terminus (T4L-β_2AR)[8]. Nb6B9 binds to the intracellular surface of the β_2AR, the G protein binding site, and stabilizes its active conformation.

The c-Epi binding site is clearly revealed by a simulated omit map suggesting that c-Epi and Epi bind in nearly identical positions (Fig. 2b). The bridging carbons that constrain Epi in c-Epi are clearly revealed by

an isomorphous difference map between the β_2AR–c-Epi data and the β_2AR-Epi data (Fig. 2b, red mesh). When comparing the β_2AR-Epi structure and β_2AR-c-Epi structure, all the orthosteric pocket residues are in similar positions (Fig. 2c). The F193[45.52] side chain is displaced slightly upward (-0.8 Å) in the c-Epi bound structure compared to the Epi bound structure, supported by the 2fofc map and isomorphous difference map between the β_2AR-c-Epi and β_2AR-Epi data (Fig. 2b). Similar upward movement of F193[45.52] is observed in the β_2AR-c-ISO structure (Supplementary Fig. 4). Even though the β_2AR-c-Epi and β_2AR-Epi structures are remarkably similar (RMSD of 0.3 Å for all Cα atoms), structure analysis suggests that c-Epi binding provides additional stabilization of ECL3 and the C-terminal end of ECL2, as revealed by a reduction in normalized b-factors (Supplementary Fig. 5).

As previously mentioned, all residues that form the orthosteric pocket (as defined within 4 Å of the ligand) of Epi are conserved between the β_2AR and the β_1AR. One residue that appears within 3.5–4.5 Å away from bridging carbons of c-Epi is Y308[7.35]. This residue is phenylalanine in the β_1AR (F359[7.35]), suggesting that the Y308[7.35]'s hydroxyl moiety could account for the affinity difference between β_2AR and the β_1AR. Substituting Y308[7.35] to phenylalanine in β_2AR, however, exhibited only a modest decrease in c-Epi affinity (Supplementary Fig. 6). Likewise, the β_1AR-F359[7.35]Y mutant displayed an almost identical affinity for c-Epi compared to the wild-type β_1AR. Taken together, these data suggest that the amino acid difference of Y/F[7.35] is not the key determinant of selectivity.

The differences in affinity observed for constrained and non-constrained catecholamines could be due to differences in agonist on-rates, off-rates, or both. We, therefore, analyzed the kinetics of c-Epi and c-NorEpi binding to both β_1AR and β_2AR. c-Epi exhibits a ~3-fold

faster association rate with the β_2AR than Epi, suggesting that conformational restriction facilitates ligand binding, probably due to entropic advantages and perhaps influenced by the increased hydrophobicity offered by the addition of the cyclic ring (Fig. 3a). Indeed, MD simulations suggest that Epi adopts a wide spectrum of conformations in the solution that rarely match its bioactive conformation, the conformation observed in the active state structure of the β_2AR bound to Epi (Fig. 2b). In contrast, c-Epi appears to exist almost exclusively in the bioactive conformation (Fig. 3b). The entropic gain that results from the conformational restriction could account for the faster association rate of c-Epi compared to Epi with the β_2AR. c-NorEpi also displays a modest ~2-fold faster association rate than NorEpi to the β_2AR, suggesting a common mechanism for differences in the association rate (Supplementary Fig. 7). The dissociation rates of both c-Epi and c-NorEpi from β_2AR were not statistically different compared to Epi or NorEpi, respectively (Fig. 3a and Supplementary Fig. 7).

In contrast, the association rates at β_1AR were significantly slower for c-Epi (~5-fold) and even slower for c-NorEpi (~15-fold) compared to the non-constrained catecholamines. The slower on-rate of c-Epi and c-NorEpi suggests that the portal to the orthosteric site on β_1AR may be less compatible with the constrained catecholamines. The faster on-rate kinetics on β_2AR are consistent with metadynamics simulations sampling of possible ligand binding pathways. While Epi adopts various compatible conformations during the process of binding to β_1AR, c-Epi does not (Fig. 3c). This is in contrast to β_2AR, where c-Epi's limited conformations appear more compatible during the process of binding to the orthosteric site (Fig. 3d). This may contribute to the slower on-rate of c-Epi compared to Epi for the β_1AR.

c-Epi or c-NorEpi also have a 2–3-fold increased dissociation rate for the β_1AR compared to Epi or NorEpi (Fig. 3a and Supplementary Fig. 7), although this difference did not reach statistical significance, it is consistent with MD simulations of c-Epi binding to the orthosteric site of β_1AR. Hydrogen bonding of the meta and para-hydroxyl on the catechol ring of catecholamines to two Ser residues on TM5 are critical for binding and efficacy on all catecholamine receptors. MD simulations show that c-Epi is much less stable in the binding pocket of the β_1AR, as revealed by a large conformational shift of the ligand in simulations and a loss of H-bonding with TM5 (Fig. 3e, f). The canonical H bond between meta-hydroxyl of c-Epi and $Ser^{5.42}$, as well as the H bond between para-hydroxyl of c-Epi and $Ser^{5.46}$ occur 76.5 and 87.5% of the time between c-Epi and the β_2AR, while the same H bonds only occur 20.8 and 21.1% of the time between c-Epi and the β_1AR (Fig. 3e, f). Thus, the lower affinity of c-Epi or c-NorEpi for the β_1AR compared to the β_2AR is thus likely due to a combined effect of ligand entropy, less compatible conformations during the binding process, and reduced stability of the ligand binding pocket.

It is important to note that the binding site modeled from crystallographic data reflects the binding site of the active conformation, which is stabilized by the G protein-mimicking nanobody. Differences in access to the orthosteric site may likely change in the active conformation compared to the inactive state. Data from pharmacological studies suggest that access to (association rate) or escape from (dissociation rate) the β_2AR orthosteric site differs significantly in the inactive and active states[11].

The role of the vestibule formed by the ECLs

The MD simulations on alprenolol binding to the β_2AR show transient interactions within the vestibule before ligand entry in the orthosteric site[6]. This was also observed in simulations following ligand binding to the muscarinic M_3 and M_4 acetylcholine receptor[12]. The vestibule on β_2AR, located directly above the orthosteric site, is composed of residues contributed by the ECLs. We previously demonstrated that replacing the ECLs of β_2AR with that of β_1AR could confer a complete switch to high-affinity NorEpi binding by accelerating the association rate[7]. With the exception of $Y308^{7.35}$ ($F359^{6.58}$ in the β_1AR), the residues

within orthosteric site of β_2AR and β_1AR that coordinate Epi binding are identical. As noted above we observed very little differences in $Y^{6.58}$ or $F^{6.58}$ in c-Epi binding. The conserved aromatic residue $F^{45.52}$ which contributes toward the formation of a lid over the orthosteric pocket drew our attention. We and others have shown that residue 45.52 affects the association and dissociation rates of ligands and arrestin signaling in other class A GPCRs[13,14]. Our structures reveal that $F193^{45.52}$ on β_2AR needs to move up by ~0.8 Å in order to accommodate the two carbons that rigidifies c-Epi. We previously showed that $F^{45.52}$, with contributions from different surrounding residues, has significant effects on NorEpi or Epi affinity[7]. The $F^{45.52}A$ mutation has a larger effect in reducing Epi and NorEpi's affinity for the β_1AR than β_2AR (~250-fold increase in Ki values for Epi and NorEpi for the β_1AR, but only a 50-fold increase for Epi and 3-fold for NorEpi for the β_2AR)[7]. In contrast, the same mutation has a larger effect in reducing c-Epi affinity for the β_2AR than β_1AR (Supplementary Fig. 8).

Analysis of the pharmacological properties of the constrained catecholamines using β_1AR-β_2AR chimeras, where the extracellular vestibules (consisting of the ECLs as well as the extracellular ends of TMs) of β_1AR and β_2AR were exchanged (Supplementary Fig. 9)[7], strongly suggests that residues within the vestibule surrounding the orthosteric pocket confer the majority of subtype selectivity of the c-Epi and c-NorEpi. As summarized in Supplemental Table 5 and Supplementary Fig. 10, replacing the extracellular vestibule of the β_2AR with that of β_1AR ($\beta_2AR_{in}/\beta_1AR_{out}$) eliminates the enhanced on-rate and accelerates the off-rates of the constrained catecholamines yielding rate constants comparable to wild-type β_1AR. Likewise, replacing the extracellular vestibule of β_1AR with that of β_2AR ($\beta_1AR_{in}/\beta_2AR_{out}$) results in a minimal change in on-rates and reduced off-rates yielding rate constants comparable to wild-type β_2AR. In agreement with the binding kinetics data, replacing the extracellular vestibule also results in the change of EC_{50} for all three constrained catecholamines in the arrestin recruitment assay (Supplementary Fig. 11).

In an attempt to pinpoint key residues within the extracellular vestibule that may contribute to the subtype selectivity offered by the constrained catecholamines, we performed mutagenesis studies to determine the role of key residues that surround $F^{45.52}$, but are not directly involved in agonist binding. Out of the residues within a 5 Å distance to $F^{45.52}$, four are different between the β_1AR and β_2AR. These are $W199^{ECL2}$, $V209^{ECL2}$, $K347^{6.58}$, and $F359^{7.35}$ in the β_1AR (Fig. 4a), and $Y174^{ECL2}$, $F194^{ECL2}$, $H296^{6.58}$, and $Y308^{7.35}$ in the β_2AR (Fig. 4b). Single point substitutions of each of the four residues on β_2AR with those of β_1AR decreased c-Epi affinity, with $F194^{ECL2}V$ having the largest effect. The reverse mutation in β_1AR, $V219^{ECL2}F$, is the only substitution out of the four that displays slightly increased c-Epi affinity. (Supplementary Fig. 12). Of note, previous studies showed that this pair of mutations (β_1AR-$V219^{ECL2}F$ and β_2AR-$F194^{ECL2}V$) had little effect on NorEpi affinity[7], suggesting that the selectivity mechanism of c-Epi for the β_2AR is different from that of NorEpi for the β_1AR.

While the individual single substitutions of the β_1AR ($W199^{ECL2}Y$, $K347^{6.58}H$, and $F359^{7.35}Y$) do not increase the receptor's affinity for c-Epi, a combination of all these three mutations together with the $V219^{ECL2}F$ (β_1AR-4mut) showed an increased c-Epi affinity qualitatively similar to the $\beta_1AR_{in}/\beta_2AR_{out}$ chimera (Fig. 4c, d, Supplementary Fig. 10, and Table 2). The results suggest that cooperation between different residues within the vestibule is required in order to establish a high-affinity c-Epi binding pocket in the β_1AR. Combining all four mutations in the β_2AR (β_2AR-4mut) shows decreased c-Epi affinity compared to wild-type β_2AR and is quantitively similar to the $\beta_2AR_{in}/\beta_1AR_{out}$ chimera (Supplementary Fig. 11 and Table 2). Interestingly, the reduced affinity of c-Epi on β_2AR-4mut was not as large as the single substitution β_2AR-$F194^{ECL2}V$, highlighting the complex behavior of the allosteric interactions between residues. We further examined the effects of the four-residue substitutions on c-NorEpi and c-ISO. In
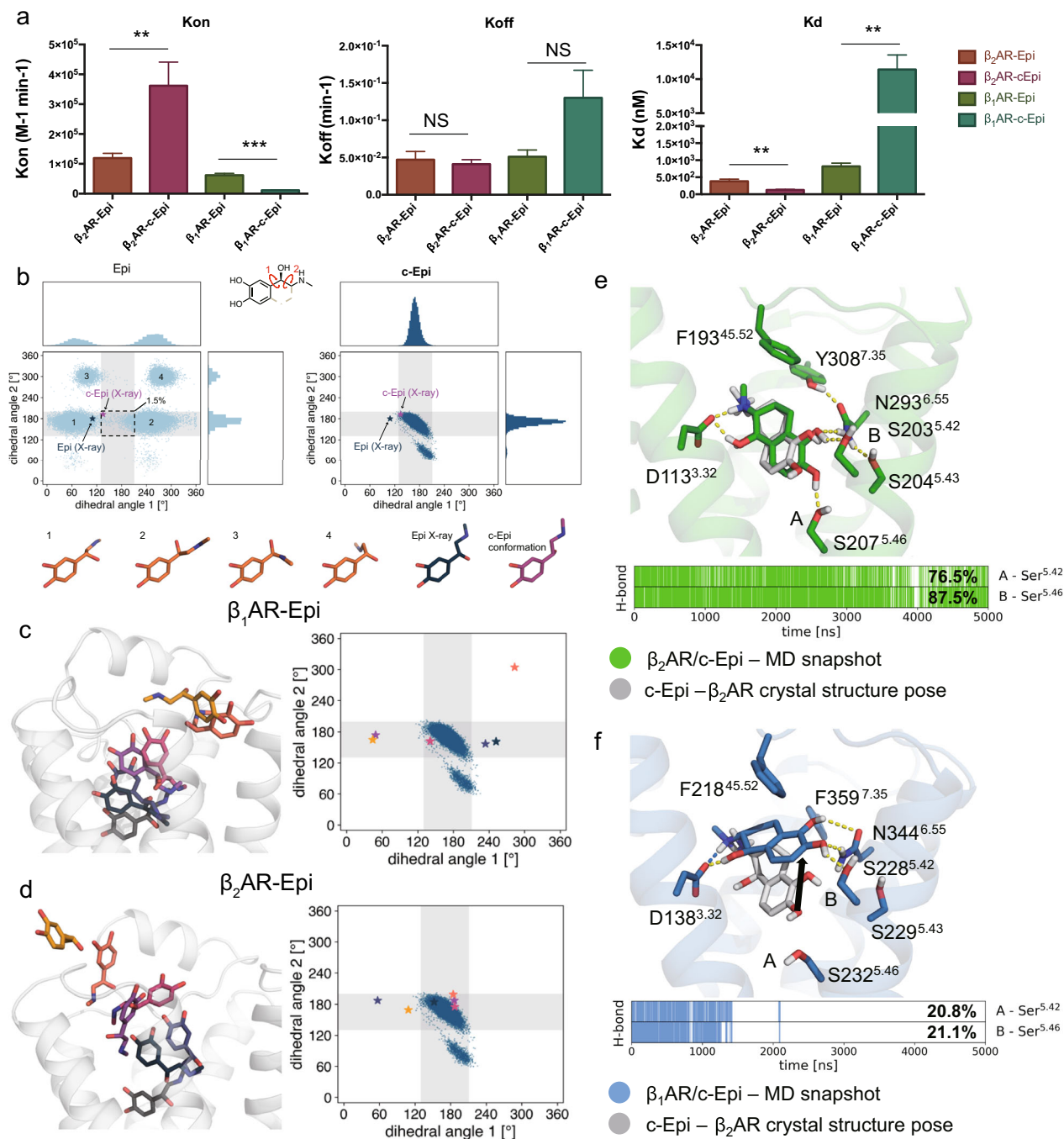
Fig. 3 | The selectivity of c-Epi toward the β₂AR reflects differences in the binding pathways and less stable orthosteric binding pocket interactions in the β₁AR. a Binding kinetics studies of Epi and c-Epi towards the β₁AR and β₂AR. Statistic analysis were performed using two-way ANOVA analysis. (*$P < 0.05$, **$P < 0.005$, ***$P < 0.0005$). Data were given as mean ± SEM of $n = 5$ (β₂AR for Epi), $n = 5$ (β₂AR for c-Epi), $n = 3$ (β₁AR for Epi), $n = 3$ (β₁AR for c-Epi), and independent experiments. Source data are provided as a Source data file. **b** MD simulations suggest that Epi adopts a wide spectrum of conformations in the solution that rarely matches its bioactive conformation, while the conformational restriction limits the catecholamine in c-Epi to the bioactive conformation. The values of two dihedral angles of the aliphatic part of Epi adopted in simulations are plotted against each other. The stars indicate the values for Epi and c-Epi as present in the β₂AR crystal structures. The dashed rectangle is a rough measure for the conformational space occupied by c-Epi in solution. The percentage value indicates the frequency by which Epi entered this space. **c, d** Epi adopts different conformations

during the binding process to the β₁AR (**c**) and β₂AR (**d**)[33]. The conformational restriction of c-Epi is incompatible with this proposed path for β₁AR, but is less so for β₂AR. The different poses of Epi represent a potential path of binding suggested by metadynamics simulations. The plot displays the dihedral angles adopted by c-Epi in solution as described for **b**. The stars show the dihedral adopted by Epi in the stages of association shown in the same color on the respective left side. **e** c-Epi maintains its crystallographic pose in the β₂AR in simulations. A representative frame of the simulations is displayed in green and the crystallographic pose of c-Epi in gray. **f** In β₁AR-c-Epi does not maintain the expected bioactive conformation in simulations. A representative frame of the simulations is displayed in blue and the crystallographic pose of c-Epi in the β₂AR in gray. **e, f** The trace plot, indicated the presence of the canonical hydrogen bonds to Ser$^{5.42}$ and Ser$^{5.46}$. The trace is displayed for one representative trajectory. The percentage value is the mean over six simulations, 5 μs each.
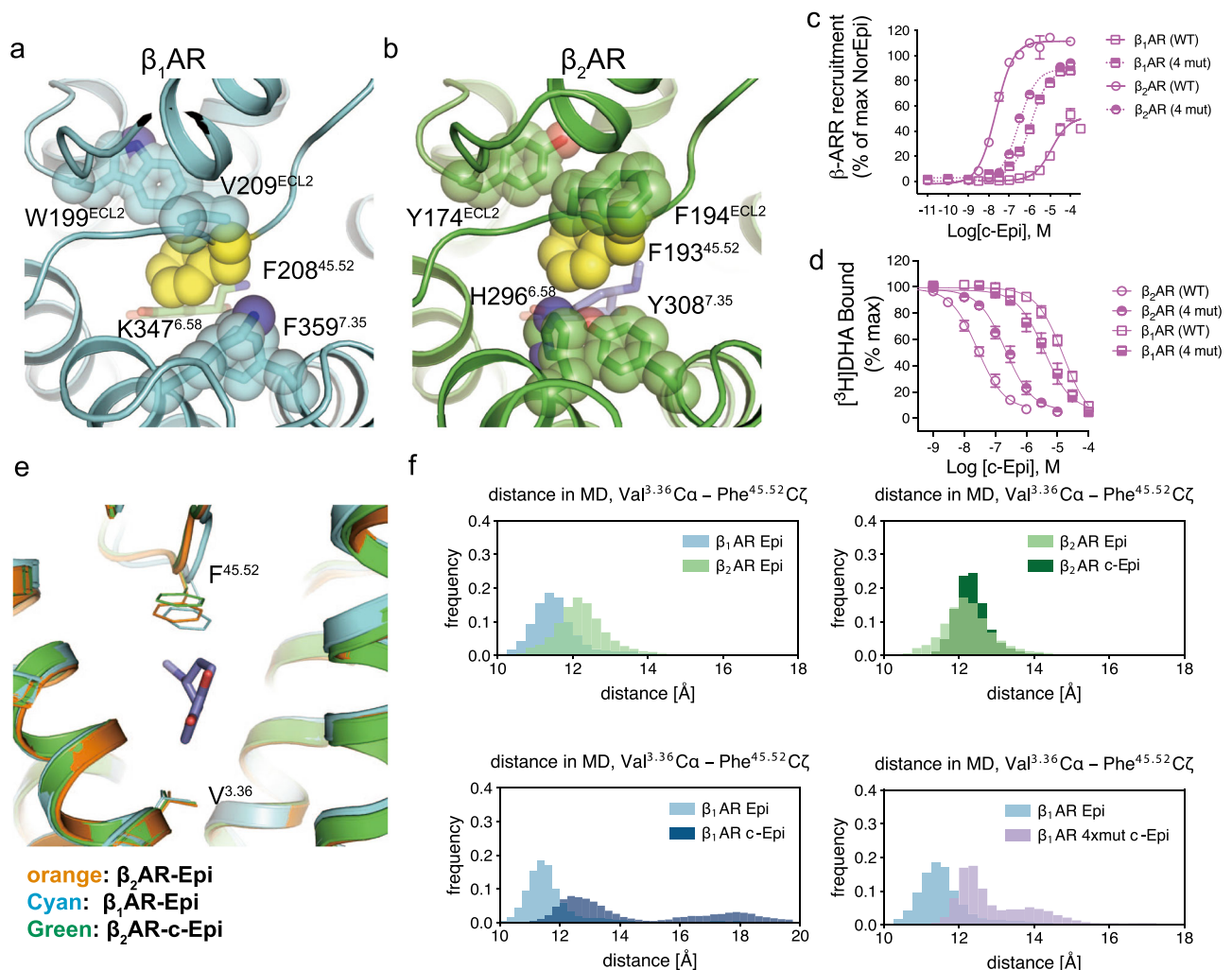
Fig. 4 | Mutating four residues around the F[45.52] affect c-Epi affinities in the β₁AR and β₂AR. a, b F[45.52] (yellow spheres) is conserved in the β₁AR and β₂AR, but is surrounded by differing residues. The different surrounding residues are W199[ECL2], V209[ECL2], K347[6.58], and F359[7.35] in the β₁AR (**a**) and Y174[ECL2], F194[ECL2], H296[6.58], and Y308[7.35] in the β₂AR (**b**). **c, d** Mutating the four residues surrounding F[45.52] reduced c-Epi affinity to the β₂AR and increased c-Epi affinity to the β₁AR, in a β-arrestin recruitment assay (**c**) and in a competition binding assay (**d**). Data were given as mean ± SEM of n = 7 (β₁AR (4 mut), β₂AR (4 mut), arrestin), n = 15 (β₁AR, arrestin), and n = 21 (β₂AR, arrestin), n = 6 (β₂AR, β₂AR, β₁AR (4 mut), β₂AR (4 mut),DHA binding) independent experiments. Source data are provided as a Source data file. **e** F[45.52] has a slightly different conformation in the β₂AR-c-Epi, β₂AR-Epi, and β₁AR-Epi structures, and as a result, the distance between V[3.36] and F[45.52] is longer in the β₂AR-c-Epi structure than in the β₂AR-Epi structure, while the distance is the shortest in the β₁AR-Epi structure. **f** The distribution for the distance between the Cα atom of V[3.36] and the Cζ atom of F[45.52] in MD simulations are displayed for the different simulation conditions. The distribution is shown in light blue for β₁AR-Epi, dark blue for β₁AR-c-Epi, light green for β₂AR-Epi, dark green for β₂AR-c-Epi and purple for β₁AR_4mut-c-Epi. Cζ of F[45.52] is located deeper in the pocket for β₁AR-Epi compared to β₂AR-Epi, and β₁AR-c-Epi shows a similar distribution as β₁AR-Epi. The deeper position in β₁AR cannot accommodate for c-Epi and leads to a distortion of the F[45.52] conformation and, therefore, to higher distances. For β₁AR_4mut-c-Epi, distances at a β₂AR-like level are observed, suggesting that the β₂AR-like surrounding of F[45.52] leads to conformations of F[45.52] that are located less deep in the pocket as for β₁AR-Epi.

arrestin recruitment assays, the β₂AR-4mut displays decreased c-NorEpi and c-ISO potency compared to the β₂AR, while β₁AR-4mut shows increased c-NorEpi and c-ISO potency compared to the β₁AR (Supplementary Fig. 13 and Supplementary Table 2).

To investigate the effect of the four-residue mutations on F[45.52] conformation and dynamics, we simulated the binding of c-Epi to β₁AR-4mut and compared the results with the MD simulations of Epi or c-Epi binding to wild-type β₁AR and β₂AR. As previously mentioned, c-Epi is not stable in the orthosteric pocket of β₁AR and the canonical H bonds between the catecholamine and TM5 are seldom observed in the simulations. With β₁AR-4mut, however, the c-Epi binding pose is more stable where canonical H bonds occur 43.9% of the time for the meta-hydroxyl and Ser[5.42] and 55.4% of the time for para-hydroxyl and Ser[5.46] (Supplementary Fig. 14a), all in good agreement with the functional data.

As observed in the crystal structure, the upward 0.8 Å movement of the F193[45.52] side chain is required in order to accommodate the extra two carbon atoms in c-Epi. In the β₂AR-Epi structure, the distance between the Cα atom of V117[3.36], which is located at the bottom of the orthosteric site, and the Cζ atom of F193[45.52] is 11 Å. In contrast, this V[3.36]/Cα – F[45.52]/Cζ distance is 11.7 Å in the β₂AR-c-Epi structure and 10.6 Å in the β₁AR-Epi structure. Similarly, MD simulations suggest that the V[3.36]/Cα – F[45.52]/Cζ distance is slightly longer in the β₂AR-c-Epi complex compared to the β₂AR-Epi complex, and slightly shorter in the β₁AR-Epi complex compared to the β₂AR-Epi complex (Fig. 4e, f). This small difference does not appear to have a major effect on the affinity of the smaller Epi, whereas the addition of the two carbons in c-Epi, requires the additional space created by the upward movement of F193[45.52]. It is likely that the allosteric effects of the residues surrounding F[45.52] in β₁AR do not permit its upward movement to the same

extent as in β_2AR without a rotamer change. MD simulations suggest that the side chain of $F^{45.52}$ in the β_1AR needs to flip away in order to avoid a clash with the c-Epi. This would require more flexibility of $F^{45.52}$ and the surrounding region of the ECL2 in the β_1AR-c-Epi simulation compared to the β_2AR-c-Epi. Substituting the four surrounding residues, as with β_1AR-4mut, results in reduced flexibility of $F^{45.52}$ and ECL2 (Supplementary Fig. 14b), displaying a similar $V^{3.36}/C\alpha - F^{45.52}/C\zeta$ distance distribution as observed in the β_2AR-c-Epi structure (Fig. 4e, f).

Of note, the $F^{45.52}$ that is crucial for high-affinity binding of the β_2AR to c-Epi is not conserved as Phe, but as branched-chain amino acids (leucine, isoleucine, valine) in the α_1AR or α_2AR subtypes (Supplementary Fig. 15a). Comparison with the $\alpha_{2B}AR$ structure (PDB code: 6K41)[15] suggests the sidechain of leucine may clash with c-Epi (Supplementary Fig. 15b). Binding studies also suggest $F^{45.52}V$ mutation decreases c-Epi affinity by ~100-fold in the β_2AR (Supplementary Fig. 8b). The difference in position 45.52 may explain the lack of activity of constrained catecholamine to the αAR subtypes.

Signaling and signal bias

In agreement with MD simulations and radioligand binding assays, the constrained catecholamines display enhanced potency on β_2AR in adenylyl cyclase assays while decreasing their potency through β_1AR stimulation (Fig. 2a). Similar enhanced effects of c-Epi and c-NorEpi were observed in β-arrestin recruitment, ie. enhanced potency on β_2AR and diminished potency at β_1AR, but with their magnitude of differences appear to be magnified in comparison to their responses in cyclase assays. Moreover, the diminished potency of the constrained catecholamines in β_1AR-promoted β-arrestin recruitment assays (19- and 25-fold decreased potency of c-Epi and c-NorEpi, respectively) is accompanied by a decreased efficacy (~50% decreased efficacy of both c-Epi and c-NorEpi). It is likely that the β_1AR, known to be a relatively poor arrestin-2 recruiter[16] for catecholamines, exhibits an even poorer response to constrained catecholamines due to a combination of suboptimal binding at the hormone-binding site, as described above, and the relative instability of the vestibule and ECLs associated with $F^{45.52}$. Thus, c-Epi and c-NorEpi confer a combined effect of lowering activity at β_1AR while improving potency at β_2AR, yielding an overall improvement in β_2AR-β_1AR selectivity.

To compare the relative effectiveness of the constrained catecholamines in cAMP and β-arrestin assays, we analyzed the dose-response relationships using an Operational Model of Bias, proposed by ref. 17. In brief, we first calculated the "transduction coefficient" of each ligand in cAMP and arrestin recruitment assays. The transduction coefficient is defined as $log(\tau/Ka)$, where τ represents the efficacy of the agonist and Ka represents the dissociation constant of the ligand (Supplementary Table 6a). Then the relative effectiveness (RE) between the two agonists were calculated as the inverse logarithm of $\Delta log(\tau/Ka)$ between these two ligands. An RE >1 implies that a new agonist, relative to a control agonist, displays superior pharmacological properties based on efficacy and affinity. The bias factors, or the comparison between the RE of the two agonists in two separate signaling assays, was calculated as the inverse logarithm of $\Delta\Delta log(\tau/Ka)$ of the same pair of agonists in two different signaling pathways (Supplementary Table 6b). In cAMP assays with β_2AR, c-Epi (RE~4), and c-NorEpi (RE ~20), compared to Epi and NorEpi, respectively, were both much higher than on β_1AR (Supplemental Table 6). In β-arrestin recruitment assays, both c-Epi and c-NorEpi appeared dramatically more effective (c-Epi: RE~21, c-NorEpi: RE ~65) compared to Epi and NorEpi, respectively. Taken together, these data suggest that both c-Epi (bias factor ~5.4) and c-NorEpi (bias factor ~3.2) on β_2AR display a signaling bias toward β-arrestin recruitment over adenylyl cyclase activity. It is important to note that although c-NorEpi displays a larger bias factor of ~ 51 on β_1AR, the relative effectiveness (RE) for c-NorEpi on β_1AR was ~2400-fold lower than NorEpi in cyclase assays and ~47-fold lower in β-arrestin recruitment assays. Interestingly, constraining

isoproterenol had a major impact on β-arrestin recruitment through β_1AR (100-fold decrease in potency compared to ISO) with little enhancing effect on β-arrestin recruitment by β_2AR. This was accompanied by only modest effects on β_1AR potency in cAMP assays and subtle effects on β_2AR-mediated efficacy. Taken together, these data suggest that constraining isoproterenol appears as a β_1AR-selective diminution, yielding a large effect on the relative effectiveness and hence biasing the signaling away from β-arrestin recruitment.

Discussion

A common goal in drug development is to target specific receptor subtypes and avoid off-target binding events that often lead to adverse side effects. However, distinguishing specific receptor subtypes that natively bind the same hormone has been a major challenge in drug discovery. Indeed, advances in the structural biology of GPCRs have provided some insight into strategies to identify subtype-selective compounds. We previously reported the development of selective antagonists for the M_3 muscarinic acetylcholine receptor and an orexin 1 receptor-selective antagonist based on single amino acid differences between these subtypes (M_3AChR and M_2AChR or OX_1R and OX_2R, respectively)[18,19]. In this study, we further show that even for GPCR subtypes like β_1AR and β_2AR that share identical orthosteric pockets, the shape and stability of the orthosteric pocket can be influenced by surrounding residues resulting in marked differences in ligand affinity.

Previous studies by ref. 20 revealed that entropy plays an important role in agonist binding to the turkey β_1AR. The authors found that isoproterenol binding to turkey red blood cell membranes was highly dependent on temperature, with higher affinity observed at lower temperatures. Antagonist binding was unaffected by temperature. The authors concluded that agonist binding is associated with an unfavorable decrease in entropy. In this current study, we designed constrained catecholamines to determine the effect of reducing the entropic penalty of binding. Of the eight possible constrained enantiomers of iso (Fig. 1c), the *(R,R)*-enantiomer bound to the β_2AR with the highest affinity. The constrained catecholamines c-NorEpi and c-Epi exhibited a faster association rate for binding to the β_2AR compared to the non-constrained agonists (Fig. 3a and Supplementary Fig. 7), consistent with a reduced entropic penalty upon binding. However, we were surprised to find that conformationally-constrained catecholamine exhibited a high degree of β_2AR selectivity, with a marked decrease in affinity for the β_1AR as well as α_1ARs and α_2ARs (Supplementary Fig. 3). This selectivity for β_2AR over β_1AR was not due to differences in the residues that directly interact with the ligand in the orthosteric binding site. Binding kinetics studies and MD simulations suggest that the difference in affinity is due to a combined effect of the loss of flexibility needed to access the orthosteric pocket of the β_1AR, and a less stable binding pose of c-Epi in the β_1AR. When comparing the β_1AR and β_2AR, we found that the position of $F^{45.52}$, common to both receptors, is slightly displaced in the β_1AR relative to the β_2AR. This difference in the orientation of $F^{45.52}$ (a smaller $V^{3.36}/C\alpha - F^{45.52}/C\zeta$ distance), which leads to a change in the shape of the binding pocket and accounting for the apparent subtype selectivity, can largely be attributed to as few as four aromatic amino acids in β_2AR ECLs that surround $F^{45.52}$.

Entropic gains with the constrained catecholamines enhanced β_2AR affinity with a simultaneous decrease in binding affinity for β_1AR, observable in ligand binding and G protein coupling assays. What was unanticipated was the greater magnitude of differences in responses in β-arrestin recruitment where the constrained catecholamines appear to have a diminutive effect on β_1AR, while enhancing the potency at β_2AR, in the case of c-Epi and c-NorEpi. Thus, constraining NorEpi completely switched the β_1AR-β_2AR selectivity from β_1AR-selective NorEpi responses to β_2AR-selective arrestin recruitment with c-NorEpi. The mechanism for the magnitude differences in β-arrestin recruitment compared to G protein or cyclase assays, ie. enhancement for

β_2AR and diminution with β_1AR, is unclear but potentially related to one clear structural difference in the catecholamine-bound β-ARs versus the constrained counterparts. Constraining the catecholamines through the addition of two carbon atoms and the formation of a second cyclic ring, impacts F[45.52] in both β_1AR and β_2AR, altering the structures of the ECLs and vestibule located above the orthosteric, hormone-binding site. Accordingly, c-Epi binding to β_1AR would require significant changes in the conformation of F[45.52] and ECL2, whereas c-Epi binding to β_2AR appears to stabilize F[45.52] and ECL2 in a conformation that favors arrestin recruitment. Indeed, previous studies on the serotonin 5-HT$_{2B}$ receptor suggest that ligands that influence the structure of ECLs appear to influence G protein and arrestin bias[13,14]. Structural data on β_2AR-arrestin complexes stabilized with c-Epi or c-NorEpi might provide some insight into how the ECLs may be involved in arrestin recruitment and hence help to delineate the basis for the observed effect on signaling bias.

Orthosteric pockets being allosterically modified by surrounding residues, such as those in the ECLs, are unlikely to be a unique case for adrenergic receptors. This study suggests that it may be possible to develop subtype-selective drugs for other GPCRs by carefully exploring the dynamics of the orthosteric pocket differences between subtypes. In this regard, high-resolution structures and MD simulations provide valuable information to guide drug development.

Methods

Protein expression and purification

A previously reported human β_2AR – T4 lysozyme fusion construct was used in this study[8]. A FLAG epitope was fused to the N-terminus. T4 lysozyme was connected to the β_2AR at position D29[1.28] with two alanine residues. The flexible ICL3 (S236-K263) was removed and the C-terminus of the receptor was truncated at position K348. The resulting T4L-β_2AR construct was expressed in Sf9 insect cells with BestBac expression systems. Purification of T4L-β_2AR and Nb6B9 were performed according to the methods described previously[8]. Briefly, Nb6B9 was purified by nickel affinity chromatography followed by size exclusion chromatography. T4L-β_2AR was solubilized with dodecylmaltoside and purified by M1-FLAG affinity chromatography followed by alprenolol functional chromatography. The elution of the alprenolol column was loaded to the M1-FLAG affinity column for ligand exchange to c-Epi and detergent exchange to L-MNG. The purified T4L-β_2AR was incubated with Nb6B9 overnight with a 1:1.5 molar ratio. The excess Nb6B9 was removed by a final size exclusion chromatography with the buffer containing 20 mM HEPES, pH 7.5, 100 mM NaCl, 0.01% MNG, 0.001% CHS, and 100 μM c-Epi. The purified T4L-β_2AR-Nb6B9-c-Epi was concentrated at 40 mg/mL and aliquoted.

Crystallization

The T4L-β_2AR-Nb6B9-c-Epi complex was reconstituted into the lipidic cubic phase with a 1:1 mass ratio of protein to lipid as previously reported[21]. The lipid stock consisted of a 10:1 mass ratio of 7.7 MAG with cholesterol. Crystals were grown using 30–100 nL drops with 1 μL of precipitant solution using a GryphonLCP robot. The crystal condition consisted of 26–31% PEG400, 100 mM MES, pH 6.2–6.7, 75–125 mM ammonium phosphate dibasic, and 1 mM c-Epi. Crystals grew after 1–3 days and were harvested for data collection.

Data collection and structure determination

The diffraction data were collected at SPring-8 beamline BL32XU. The micro-focused beam with 10 μm × 15 μm size and 1.0 Å wavelength was used for automatic data collection[22]. For each crystal, a 10° dataset was collected with 0.1° oscillation per frame. Automatic data processing was performed by KAMO[23]. Fifty-eight crystals were merged to generate the final 3.1 Å T4L-β_2AR-Nb6B9-c-Epi dataset and 43 crystals were merged to generate the final 3.4 Å T4L-β_2AR-Nb6B9-c-ISO dataset. The structure of the T4L-β_2AR-Nb6B9-c-Epi complex was solved by

molecular replacement method with PHENIX[24] and T4L-β_2AR-Nb6B9-Epinephrine structure (PDE code: 4LDO) as the search model. Structure refinement was carried out with PHENIX and COOT. Molprobity[25] was used to validate the final structure. The statistics for data collection and structure refinement were summarized in Supplementary Table 7. The structure figures were prepared using PyMol (The PyMOL Molecular Graphics System, Schrodinger, LLC).

The isomorphous difference map was calculated using FFT[26] in CCP4[27]. In brief, the T4L-β_2AR-Nb6B9-c-Epi data and the T4L-β_2AR-Nb6B9-Epi data were set to the same scale and a Fo-Fo difference map was calculated by subtracting the T4L-β_2AR-Nb6B9-Epi from the T4L-β_2AR-Nb6B9-c-Epi data.

Normalized b-factor was calculated by dividing the b-factor of each residue by the overall b-factor of the receptor. To visualize the b-factor change, the residue is colored blue if the normalized b-factor is smaller in the β_2AR-Nb6B9-c-Epi structure than in the β_2AR-Nb6B9-Epi structure, and colored in red if the normalized b-factor is larger in the β_2AR-Nb6B9-c-Epi structure than in the β_2AR-Nb6B9-Epi structure. The darkness of blue or red color correlates with how large the normalized b-factor difference is between the two structures.

Radioligand binding

The wild-type and mutated human β_2AR and β_1AR constructs were cloned into pFastbac vector and expressed in Sf9 cells with a Bac-to-Bac expression system. The cell membrane was isolated and resuspended with a binding buffer consisting of 20 mM HEPES, pH 7.5, and 100 mM NaCl. For competition binding assays, the diluted membrane was incubated for 2 h with various concentrations of cold ligands and 2 nM [^{3}H]DHA in the cold binding buffer containing 0.5% BSA to a final volume of 500 μL. The membrane filtration was performed with Brandel 48-well harvester and the collected filter papers and membranes were incubated with OptiPhase HiFafe 3 liquid scintillation cocktail. The Microbeta2 scintillation counter was used for radioactivity counting. The competition binding curves were fitted by GraphPad Prism 6.0 (GraphPad LLC, CA).

Cloning

The human β_1AR, β_2AR, α1A, α1B, β_1AR_mut4, β_2AR_mut4, and the murine α2A receptor were fused to the PK1 sequence, the α2B and α2C receptor to ARMS2-PK2 and all cloned to pCMV (DiscoverX, Eurofins) for β-arrestin-2 recruitment assays, respectively, using polymerase chain reaction and Gibson Assembly (New England Biolabs)[28]. Sequence integrity was verified by DNA sequencing (Eurofins Genomics). The β_1AR/β_2AR chimeras were generated by switching the N-terminus of the receptors as well as 55 residues between W[1.31] and the C-terminus of the receptor. The detailed sequences were shown in Supplementary Figure 9, which is modified from a previous publication from our group[7].

Radioligand binding assay with membranes from HEK cells

Binding affinities towards the human β_1AR and β_2AR were determined as described previously[29,30]. In brief, membranes were prepared from HEK293T cells transiently transfected with the cDNA for β_1AR and β_2AR (obtained from the cDNA resource center, www.cdna.org). Receptor densities (B$_{max}$ value) and specific binding affinities (K_D value) for the radioligand [^{3}H]CGP12,177 (specific activity 51 Ci/mmol, PerkinElmer, Rodgau, Germany) were determined as 4.3 ± 1.1 pmol/mg protein and 0.125 ± 0.032 nM for β_1AR and 2.7 ± 0.4 pmol/mg protein and 0.080 ± 0.011 nM for β_2AR, respectively. Competition binding experiments were performed by incubating membranes in binding buffer (25 mM HEPES, 5 mM MgCl$_2$, 1 mM EDTA, and 0.006% bovine serum albumin at pH 7.4) at a final protein concentration of 2–6 μg/well, together with the radioligand (final concentration 0.2–0.3 nM) and varying concentrations of the competing ligands for 60 min at 37 °C. Non-specific binding was determined in the presence of unlabeled

CGP12,177 at a final concentration of 10 μM. Protein concentration was established using the method of ref. 31.

The resulting competition curves were analyzed by nonlinear regression using the algorithms implemented in PRISM 8.0 (GraphPad Software, San Diego, CA) to provide an IC_{50} value, which was subsequently transformed into a K_i value employing the equation of Cheng and Prusoff [32]. Mean K_i values (±SEM) were derived from 3 to 14 experiments, each performed in triplicates.

The binding kinetics assay

The binding kinetics assays were performed as previously described in ref. 7. In brief, off-rate measurements in membranes containing the target receptors (the human β_1AR, β_2AR as well as the $\beta_1AR_{in}/\beta_2AR_{out}$ and $\beta_2AR_{in}/\beta_1AR_{out}$ chimeras) were pre-incubated with 0.1–0.5 nM [³H] DHA for 1 h at RT. [³H]DHA dissociation rates were initiated with the addition of excess propranolol (50 μM) and samples were subjected to rapid filtration at various times. Association rates were determined by incubating membranes with [³H]DHA (ranging from 0.1–0.5 nM concentration) in the absence or presence of three different concentrations of (3, 10, and 30 μM NorEpi for β_2AR; 0.3, 1, and 3 μM NorEpi for β_1AR; 3, 10, and 30 μM NorEpi for $\beta_1AR_{in}/\beta_2AR_{out}$; 0.3, 1, and 3 μM NorEpi for $\beta_2AR_{in}/\beta_1AR_{out}$; 1, 3, and 10 μM c-NorEpi on β_2AR; 3, 10, and 30 μM c-NorEpi for β_1AR; 1, 3, and 10 μM c-NorEpi on β_1AR and β_2AR; 3, 10, and 30 μM c-NorEpi for $\beta_1AR_{in}/\beta_2AR_{out}$; 1, 3, and 10 μM c-NorEpi on $\beta_2AR_{in}/\beta_1AR_{out}$; 0.3, 1, and 3 μM Epi for β_2AR; 1, 3, and 10 μM Epi on β_1AR; 0.3, 1, and 3 μM Epi for $\beta_2AR_{in}/\beta_1AR_{out}$; 3, 10, and 30 μM Epi for $\beta_1AR_{in}/\beta_2AR_{out}$; 3, 10, and 30 μM; c-Epi for β_1AR; 0.1, 0.3, and 1 μM; c-Epi for β_2AR; 3, 10, and 30 μM c-Epi for $\beta_2AR_{in}/\beta_1AR_{out}$; 3, 10, and 30 μM c-Epi for $\beta_1AR_{in}/\beta_2AR_{out}$) the catecholamine. Aliquots were removed at various times and subjected to rapid filtration. Membranes containing bound [³H]DHA were harvested by filtering through GF/C Unifilter™ (Perkin Elmer) and counted on a Top Count™ (Perkin Elmer) scintillation counter. Binding kinetics were calculated using the Kinetics of Competitive Binding fit in GraphPad Prism 6.0 (GraphPad LLC, CA). The kinetics parameters of [³H]DHA used in the analysis were derived from a previous study [7].

β-Arrestin-2 recruitment and G protein IP-one assay

Determination of receptor-stimulated β-arrestin-2 recruitment was performed applying the PathHunter assay (DiscoverX, Birmingham, UK), which is based on the measurement of fragment complementation of β-galactosidase as described in ref. 33. In detail, HEK293T cells stably expressing the enzyme acceptor (EA) tagged β-arrestin-2 fusion protein were transfected with the cDNA for β_1AR, β_2AR, β_1AR_mut4, β_2AR_mut4, α1A, α1B, or α2A receptor each fused to the ProLink-PK1 fragment for enzyme complementation and transferred into 384 well microplates. α2B and α2C receptors fused to the ProLink-ARMS2-PK2 fragment were treated analogously. Measurement started by incubating cells with agonist for 90 min (β_1AR, β_2AR, β_2AR_mut4, α2B, or α2C, respectively), 180 min (β_1AR_mut4, α1B, or α2A, respectively), or 300 min (α1A), respectively. Chemoluminescence was monitored with a Clariostar plate reader (BMG, Ortenberg, Germany) and analyzed by normalizing the raw data relative to basal activity (0%) and the maximum effect of Norepi (100%). Four to 21 repeats in duplicate were analyzed by applying the algorithms for four-parameter nonlinear regression implemented in Prism 8.0 (GraphPad LLC, CA) to get dose-response curves representing EC_{50} and E_{max} value. Bias calculations were performed as described by ref. 17.

The determination of receptor-mediated G protein signaling by β_1AR and β_2AR was performed by applying an IP accumulation assay (IP-One HTRF®, Cisbio, Codolet, France) according to the manufacturer's protocol and in analogy to previously described protocols [18]. In brief, HEK 293 T cells were co-transfected with the cDNA for β_1AR or β_2AR and the hybrid G protein Gαqs (Gαq protein with the last five amino acids at the C-terminus replaced by the corresponding

sequence of Gαs (gift from The J. David Gladstone Institutes, San Francisco, CA), respectively and transferred into 384 well microplates. Cells were incubated with an agonist for 120 min and accumulation of the second messenger was stopped by adding detection reagents (IP1-d2 conjugate and Anti-IP1cryptate TB conjugate). After 60 min, TR-FRET was measured with a Clariostar plate reader. FRET-signals from four to 14 repeats in duplicates were normalized to vehicle (0%) and the maximum effect of Norepi (100%) and analyzed to get EC_{50} and E_{max} values.

cAMP accumulation assay

Initial cAMP assays on β_2AR were performed using clonal selected HEK293 ΔGNAS cell line [34], stably expressing the cAMP biosensor pink flamido [35] (encoded on a pcDNA4.0/TO/Zeocin plasmid, generously provided by Dr. Jin Zhang, UCSD). Briefly, cells were treated with 4 μg/mL doxycycline to induce overexpression of the cAMP biosensor 48 h prior to measurement of cAMP. Cells were gently harvested, washed in Hanks' Balanced Salt Solution (HBSS, Sigma), and seeded onto clear bottom poly-D-lysine coated, black 96-well polystyrene assay plate (Costar) at -2 × 10⁶ cells per well. Cells were treated with a dilution series of catecholamine (10⁻⁴–10⁻¹⁰ M) in HBSS buffer with 20 mM HEPES, pH 7.8, 600 μM 3-Isobutyl-1-methylxanthine (IBMX), and 3 mM ascorbic acid. Real-time fluorescence measurements were collected immediately following agonist application: excitation 535 nm, emission 612 nm, integration time 40 μs, bottom read, a kinetic interval of 13 s, and a delay of 10 ms using a fluorescence plate reader (BioTek, Winooski, VT). The cAMP accumulation was monitored for 17.5 min. The fluorescence emission data were fitted to a single exponential to obtain rate constants (from $t = 5$ s to $t = 305$ s) for each agonist concentration using Prizm (GraphPad LLC, CA). Rate constants were plotted as a function of catecholamine concentration and fitted to a logistics curve using Prism.

Subsequent cAMP assays on β_1AR and β_2AR were performed in *Sf9* cells. Briefly, cells were infected with baculoviruses for the cAMP biosensor pink flamido, together with either β_1AR or β_2AR. Twenty-four hours following infection, cells were gently harvested, washed in HBSS, and seeded onto clear bottom poly-D-lysine coated, black 96-well polystyrene assay plate (Costar) at -1 × 10⁶ cells per well. Cells were treated with a dilution series of catecholamine (10⁻⁴–10⁻¹⁰ M) in HBSS buffer with 20 mM HEPES, pH 7.8, 600 μM IBMX, and 3 mM ascorbic acid. Real-time fluorescence measurements were collected immediately following agonist application: excitation 535 nm, emission 612 nm, integration time 40 μs, bottom read, a kinetic interval of 13 s, and a delay of 10 ms using a fluorescence plate reader (SpectraMax M5, Molecular Devices, CA). The cAMP accumulation was monitored for 10 min. The fluorescence emission data were fitted to a single exponential to obtain rate constants (from $t = 5$ s to $t = 305$ s) for each agonist concentration using Prizm (GraphPad LLC, CA). Rate constants were plotted as a function of catecholamine concentration and fitted to a logistics curve using Prism. All statistical analysis for EC_{50} and E_{max}, as well as relative effectiveness and bias, was performed using Prism. Relative effectiveness and Bias calculations were performed as described by ref. 17.

[³⁵S]GTPγS binding assays

Membranes were prepared from *Sf*9 cells expressing Gαsβ1γ2 and β_2AR. Membranes (-15 μg) were pretreated with GDP (final assay concentration of 1 μM) in a GTPγS assay buffer (20 mM HEPES, pH 7.4, 100 mM NaCl, 10 mM MgCl₂, and 1 mM ascorbic acid) and different concentrations of agonist (Epi, c-Epi, NorEpi, c-NorEpi, Iso or c-Iso) for 10 min at room temperature before adding [³⁵S]GTPγS (for a final concentration of 0.1 nM). The assay was incubated at 30 °C for 30 min before stopping by rapid filtration through GF/B Unifilter plates (Whatman) and washing with ice-cold assay buffer. Filter plates were dried before adding Microscint 0™ and counting bound [³⁵S]GTPγS

(Perkin Elmer) using a TopCount™ (Perkin Elmer). Data were analyzed using Prizm 6.0 (GraphPad, LLC, CA). Figures show the combined results from three separate experiments performed in duplicate.

Unbiased simulations of receptor-ligand complexes

Simulations of β_2AR were based on the c-Epi bound crystal structure described in this manuscript and the epinephrine-bound crystal structure (PDB entry 4LDO)[8]. Simulations of β_1AR were based on a BI-167107 bound crystal structure of β_1AR (PDB entry 7BU7)[7]. For the simulations of β_1AR, BI-167107 was replaced with either Epi or c-Epi by structurally aligning the crystal structures β_1AR and the respective β_2AR and transferring the coordinates of the ligands. Mutations to β_1AR were introduced utilizing Maestro (Schrödinger, LCC, New York, NY, 2018) while selecting the rotamers with the highest probability and at the same time, resembling the respective conformation in the c-Epi bound β_2AR crystal structure.

Coordinates were prepared by removing the nanobody and the T4L fusion protein. Only crystal waters within or close to the receptor were retained. Prime (Schrödinger, LCC, New York, NY, 2018) was used to model missing side chains. Hydrogen atoms were added, and the protein chain termini were capped with the neutral acetyl and methyl amide groups.

Except for $D^{2.50}$, $E^{3.41}$, and $D^{3.49}$, all titratable residues were left in their dominant protonation state at pH 7.0. Previous studies suggested that residues $D^{2.50}$ and $D^{3.49}$ for β_2AR are protonated in the active state[36,37], and residue $E^{3.41}$ directly contacts the lipid interface and, therefore, will also exist predominantly in its protonated state[38,39]. We thus protonated these three residues in our simulations. Epi and c-Epi were protonated at the secondary amine allowing the formation of the canonical salt bridge to $D^{3.32}$ conserved in aminergic GPCRs.

The prepared protein structures were then aligned to the Orientation of Proteins in Membranes (OPM)[40] structure of active β_2AR (PDB entry 3SN6) and internal water was added utilizing Dowser[41]. Each complex was inserted into a pre-equilibrated bilayer of palmitoyl-oleoyl-phosphatidylcholine (POPC) lipids using Dabble, a simulation preparation software (Betz, R. Dabble (v.2.6.3). https://doi.org/10.5281/zenodo.836914 (2017)). Sodium and chloride ions were added to neutralize each system at a concentration of approximately 150 mM. The final box dimensions were approximately $85 \times 75 \times 85 \, \text{Å}^3$.

We used the CHARMM36m[42–46] parameter set for protein molecules, lipid molecules, and salt ions and the CHARMM TIP3P model for water. Parameters for Epi and c-Epi were generated using the CHARMM General Force Field (CGenFF)[47–49] with the ParamChem server (paramchem.org) version 1.0.0.

We performed the simulations using the CUDA version of PMEMD (particle-mesh Ewald molecular dynamics) in AMBER16[50]. We performed six independent simulations under each condition. Each simulation was equilibrated independently as follows: Three rounds of minimization were performed, each consisting of 500 iterations of steepest descent minimization, followed by 500 iterations of conjugate gradient descent minimization, with harmonic restraints of 10.0, 5.0, and 1.0 kcal mol^{-1} Å^{-2} placed on the protein and lipids, respectively. Systems were heated from 0 to 100 K in the NVT ensemble over 12.5 ps and then from 100 to 310 K in the NPT ensemble over 125 ps, using 10.0 kcal mol^{-1} Å^{-2} harmonic restraints applied to lipid and protein-heavy atoms. Systems were then equilibrated at 310 K in the NPT ensemble at 1 bar, with harmonic restraints on all protein-heavy atoms for 10 ns. Starting at 5.0 kcal mol^{-1} Å^{-2}, the restraints were reduced in a stepwise fashion by 1.0 kcal mol^{-1} Å^{-2} every 2 ns. This was followed by additional 20 ns of equilibration with again harmonic restraints on all protein-heavy atoms. Starting at 1.0 kcal mol^{-1} Å^{-2}, the restraints were reduced in a stepwise fashion by 0.1 kcal mol^{-1} Å^{-2} every 2 ns. Production simulations were performed in the NPT ensemble at 310 K and 1 bar, using a Langevin thermostat for temperature coupling and a Monte Carlo barostat for pressure coupling. These simulations used a 4 fs time step with hydrogen mass repartitioning[51]. Bond lengths to hydrogen atoms were constrained using SHAKE[52]. Periodic boundary conditions were applied. Non-bonded interactions were cut off at 9.0 Å, and long-range electrostatic interactions were computed using particle-mesh Ewald (PME)[53] with an Ewald coefficient of approximately 0.31 Å and an interpolation order of four. The fast Fourier transform (FFT) grid size was chosen such that the width of a grid cell was ~1 Å.

During production simulations, all residues within 5 Å of the G protein interface at β_2AR were restrained to the initial structure using 5.0 kcal mol^{-1} Å^{-2} harmonic restraints applied to non-hydrogen atoms. Using such restraints instead of the intracellular binding partner reduces the overall system size, enabling faster simulation, while ensuring that the receptor maintains an active conformation throughout the simulation.

Trajectory snapshots were saved every 200 ps during production simulations. Analysis of the trajectories was performed using Visual Molecular Dynamics (VMD)[54], CPPTRAJ[55], and GetContacts (https://getcontacts.github.io/). Root-mean-square fluctuations (rmsf) were calculated to an average structure omitting the first 500 ns of each simulation trajectory to avoid including any initial relaxation or equilibration of the system. Trajectories were aligned to the initial crystal structure on all transmembrane helix alpha carbons. For each simulation condition, an average structure was generated by considering trajectory snapshots from all simulations under that condition. The rmfs for each alpha carbon was then calculated for each trajectory under that condition relative to this average position using CPPTRAJ. Visualization was performed using the PyMOL Molecular Graphics System, Version 2.1.1 (Schrödinger, LLC). Plots were created using Matplotlib 3.0.2[56].

Unbiased simulations of ligands in solution

Parameter topology and coordinate files were built up using the tleap module of AMBER18[57]. For the simulations, the general AMBER force field (GAFF)[58] was used for Epi and c-Epi. The ligands were solvated in a truncated octahedron with a minimum solute-to-wall distance of 25 Å. The systems were neutralized with one chloride ion. The TIP3P water model[59] was applied. Parameters for Epi and c-Epi were assigned using antechamber[57]. The structure of Epi and c-Epi were optimized using Gaussian 16[60] at the B3LYP/6-31 G(d) level of theory and charges were calculated at HF/6-31 G(d) level of theory. Subsequently, atom point charges were assigned according to the RESP procedure[61]. A formal charge of +1 was assigned to Epi and c-Epi.

We performed the simulations using the CUDA version of PMEMD in AMBER18[57]. Each simulation system was energy minimized 2500 iterations of steepest descent minimization, followed by 7500 iterations of conjugate gradient descent minimization and equilibrated in the NVT ensemble at 310 K for 1 ns followed by the NPT ensemble for 1 ns with harmonic restraints of 10.0 kcal mol^{-1} on the ligand. In the NVT ensemble, the Langevin thermostat was used. In the NPT ensemble, the Monte Carlo barostat was applied. The system was further equilibrated for 12 ns with restraints on the ligand atoms. Here, the restraints were reduced every 3 ns in a stepwise fashion to be 5.0, 1.0, 0.5, and 0.1 kcal mol^{-1}, respectively. Productive simulations were performed using periodic boundary conditions and a time step of 2 fs. Bond lengths to hydrogen atoms were constrained using SHAKE[52]. Long-range electrostatic interactions were computed using the PME[53] method. Non-bonded interactions were cut off at 8.0 Å.

Trajectory snapshots were saved every 50 ps during production simulations. Trajectories were visualized using VMD[54] and cluster based on the ligand atoms using the CPPTRAJ[55] module of AMBER18. Visualization was performed using PyMOL Molecular Graphics System, Version 2.1.1 (Schrödinger, LLC). Plots were created using Matplotlib 3.0.2[56].

Reporting summary

Further information on research design is available in the Nature Portfolio Reporting Summary linked to this article.

Data availability

The coordinates and structural factors of T4L-β_2AR/NB6B9/c-Epi and T4L-β_2AR/NB6B9/c-ISO structures have been deposited into Protein Data Bank under the accession code 7XKA (T4L-β_2AR/NB6B9/c-Epi structure) and 7XK9 (T4L-β_2AR/NB6B9/c-ISO structure), respectively. Source data are provided with this paper.

References

1. Sriram, K. & Insel, P. A. G protein-coupled receptors as targets for approved drugs: how many targets and how many drugs. *Mol. Pharm.* **93**, 251–258 (2018).
2. Chan, H. C. S., Li, Y., Dahoun, T., Vogel, H. & Yuan, S. New binding sites, new opportunities for GPCR drug discovery. *Trends Biochem. Sci.* **44**, 312–330 (2019).
3. Ogrodowczyk, M., Dettlaff, K. & Jelinska, A. Beta-blockers: current state of knowledge and perspectives. *Mini Rev. Med. Chem.* **16**, 40–54 (2016).
4. Billington, C. K., Penn, R. B. & Hall, I. P. β(2) agonists. *Handb. Exp. Pharm.* **237**, 23–40 (2017).
5. Minneman, K. P., Pittman, R. N. & Molinoff, P. B. Beta-adrenergic receptor subtypes: properties, distribution, and regulation. *Annu. Rev. Neurosci.* **4**, 419–461 (1981).
6. Dror, R. O. et al. Pathway and mechanism of drug binding to G-protein-coupled receptors. *Proc. Natl Acad. Sci. USA* **108**, 13118–13123 (2011).
7. Xu, X. et al. Binding pathway determines norepinephrine selectivity for the human beta1AR over beta2AR. *Cell Res.* **31**, 569–579 (2021).
8. Ring, A. M. et al. Adrenaline-activated structure of beta2-adrenoceptor stabilized by an engineered nanobody. *Nature* **502**, 575–579 (2013).
9. Warne, T., Edwards, P. C., Dore, A. S., Leslie, A. G. W. & Tate, C. G. Molecular basis for high-affinity agonist binding in GPCRs. *Science* **364**, 775–778 (2019).
10. Nishikawa, M. et al. Selective beta-adrenoceptor activities of tetrahydronaphthalene derivatives. *Life Sci.* **16**, 305–314 (1975).
11. DeVree, B. T. et al. Allosteric coupling from G protein to the agonist-binding pocket in GPCRs. *Nature* **535**, 182–186 (2016).
12. Kenakin, T. & Strachan, R. T. PAM-antagonists: a better way to block pathological receptor signaling. *Trends Pharm. Sci.* **39**, 748–765 (2018).
13. Wacker, D. et al. Crystal structure of an LSD-bound human serotonin receptor. *Cell* **168**, 377 (2017).
14. McCorvy, J. D. et al. Structure-inspired design of beta-arrestin-biased ligands for aminergic GPCRs. *Nat. Chem. Biol.* **14**, 126–134 (2018).
15. Yuan, D. et al. Activation of the alpha2B adrenoceptor by the sedative sympatholytic dexmedetomidine. *Nat. Chem. Biol.* **16**, 507–512 (2020).
16. Shiina, T., Kawasaki, A., Nagao, T. & Kurose, H. Interaction with beta-arrestin determines the difference in internalization behavior between beta1- and beta2-adrenergic receptors. *J. Biol. Chem.* **275**, 29082–29090 (2000).
17. van der Westhuizen, E. T., Breton, B., Christopoulos, A. & Bouvier, M. Quantification of ligand bias for clinically relevant beta2-adrenergic receptor ligands: implications for drug taxonomy. *Mol. Pharm.* **85**, 492–509 (2014).
18. Liu, H. et al. Structure-guided development of selective M3 muscarinic acetylcholine receptor antagonists. *Proc. Natl Acad. Sci. USA* **115**, 12046–12050 (2018).
19. Hellmann, J. et al. Structure-based development of a subtype-selective orexin 1 receptor antagonist. *Proc. Natl Acad. Sci. USA* **117**, 18059–18067 (2020).
20. Weiland, G. A., Minneman, K. P. & Molinoff, P. B. Fundamental difference between the molecular interactions of agonists and antagonists with the beta-adrenergic receptor. *Nature* **281**, 114–117 (1979).
21. Caffrey, M. & Cherezov, V. Crystallizing membrane proteins using lipidic mesophases. *Nat. Protoc.* **4**, 706–731 (2009).
22. Hirata, K. et al. ZOO: an automatic data-collection system for high-throughput structure analysis in protein microcrystallography. *Acta Crystallogr. D. Struct. Biol.* **75**, 138–150 (2019).
23. Yamashita, K., Hirata, K. & Yamamoto, M. KAMO: towards automated data processing for microcrystals. *Acta Crystallogr. D. Struct. Biol.* **74**, 441–449 (2018).
24. Adams, P. D. et al. PHENIX: a comprehensive Python-based system for macromolecular structure solution. *Acta Crystallogr. Sect. D. Biol. Crystallogr.* **66**, 213–221 (2010).
25. Chen, V. B. et al. MolProbity: all-atom structure validation for macromolecular crystallography. *Acta Crystallogr. Sect. D. Biol. Crystallogr.* **66**, 12–21 (2010).
26. Ten Eyck, L. F. Fast Fourier transform calculation of electron density maps. *Methods Enzymol.* **115**, 324–337 (1985).
27. Winn, M. D. et al. Overview of the CCP4 suite and current developments. *Acta Crystallogr. Sect. D., Biol. Crystallogr.* **67**, 235–242 (2011).
28. Gibson, D. G. et al. Enzymatic assembly of DNA molecules up to several hundred kilobases. *Nat. Methods* **6**, 343–345 (2009).
29. Stanek, M. et al. Hybridization of beta-adrenergic agonists and antagonists confers G protein bias. *J. Med Chem.* **62**, 5111–5131 (2019).
30. Hubner, H. et al. Structure-guided development of heterodimer-selective GPCR ligands. *Nat. Commun.* **7**, 12298 (2016).
31. Lowry, O. H., Rosebrough, N. J., Farr, A. L. & Randall, R. J. Protein measurement with the Folin phenol reagent. *J. Biol. Chem.* **193**, 265–275 (1951).
32. Cheng, Y. & Prusoff, W. H. Relationship between the inhibition constant (K1) and the concentration of inhibitor which causes 50 per cent inhibition (I50) of an enzymatic reaction. *Biochem. Pharm.* **22**, 3099–3108 (1973).
33. Liu, X. et al. An allosteric modulator binds to a conformational hub in the beta2 adrenergic receptor. *Nat. Chem. Biol.* **16**, 749–755 (2020).
34. Stallaert, W. et al. Purinergic receptor transactivation by the beta2-adrenergic receptor increases intracellular Ca(2+) in nonexcitable cells. *Mol. Pharm.* **91**, 533–544 (2017).
35. Harada, K. et al. Red fluorescent protein-based cAMP indicator applicable to optogenetics and in vivo imaging. *Sci. Rep.* **7**, 7351 (2017).
36. Ghanouni, P. et al. The effect of pH on beta(2) adrenoceptor function. Evidence for protonation-dependent activation. *J. Biol. Chem.* **275**, 3121–3127 (2000).
37. Ranganathan, A., Dror, R. O. & Carlsson, J. Insights into the role of Asp79(2.50) in beta2 adrenergic receptor activation from molecular dynamics simulations. *Biochemistry* **53**, 7283–7296 (2014).
38. Dror, R. O. et al. Identification of two distinct inactive conformations of the beta2-adrenergic receptor reconciles structural and biochemical observations. *Proc. Natl Acad. Sci. USA* **106**, 4689–4694 (2009).
39. Rosenbaum, D. M. et al. Structure and function of an irreversible agonist-beta(2) adrenoceptor complex. *Nature* **469**, 236–240 (2011).
40. Lomize, M. A., Lomize, A. L., Pogozheva, I. D. & Mosberg, H. I. OPM: orientations of proteins in membranes database. *Bioinformatics* **22**, 623–625 (2006).
41. Zhang, L. & Hermans, J. Hydrophilicity of cavities in proteins. *Proteins* **24**, 433–438 (1996).

42. Best, R. B., Mittal, J., Feig, M. & MacKerell, A. D. Jr. Inclusion of many-body effects in the additive CHARMM protein CMAP potential results in enhanced cooperativity of α-helix and β-hairpin formation. *Biophys. J.* **103**, 1045–1051 (2012).

43. Best, R. B. et al. Optimization of the additive CHARMM all-atom protein force field targeting improved sampling of the backbone φ, ψ and side-chain χ(1) and χ(2) dihedral angles. *J. Chem. Theory Comput* **8**, 3257–3273 (2012).

44. Huang, J. & MacKerell, A. D. Jr. CHARMM36 all-atom additive protein force field: validation based on comparison to NMR data. *J. Comput. Chem.* **34**, 2135–2145 (2013).

45. Klauda, J. B. et al. Update of the CHARMM all-atom additive force field for lipids: validation on six lipid types. *J. Phys. Chem. B* **114**, 7830–7843 (2010).

46. Huang, J. et al. CHARMM36m: an improved force field for folded and intrinsically disordered proteins. *Nat. Methods* **14**, 71–73 (2017).

47. Vanommeslaeghe, K. et al. CHARMM general force field: a force field for drug-like molecules compatible with the CHARMM all-atom additive biological force fields. *J. Comput. Chem.* **31**, 671–690 (2010).

48. Vanommeslaeghe, K., Raman, E. P. & MacKerell, A. D. Jr. Automation of the CHARMM general force field (CGenFF) II: assignment of bonded parameters and partial atomic charges. *J. Chem. Inf. Model* **52**, 3155–3168 (2012).

49. Vanommeslaeghe, K. & MacKerell, A. D. Jr. Automation of the CHARMM general force field (CGenFF) I: bond perception and atom typing. *J. Chem. Inf. Model* **52**, 3144–3154 (2012).

50. Case, D. A. et al. AMBER 2016. University of California, San Francisco (2016).

51. Hopkins, C. W., Le Grand, S., Walker, R. C. & Roitberg, A. E. Long-time-step molecular dynamics through hydrogen mass repartitioning. *J. Chem. Theory Comput.* **11**, 1864–1874 (2015).

52. Ryckaert, J.-P., Ciccotti, G. & Berendsen, H. J. C. Numerical integration of the cartesian equations of motion of a system with constraints: molecular dynamics of n-alkanes. *J. Comput. Phys.* **23**, 327–341 (1977).

53. Darden, T., York, D. & Pedersen, L. Particle mesh Ewald - an N.Log(N) method for Ewald sums in large systems. *J. Chem. Phys.* **98**, 10089–10092 (1993).

54. Humphrey, W., Dalke, A. & Schulten, K. VMD: visual molecular dynamics. *J. Mol. Graph* **14**, 27–38 (1996).

55. Roe, D. R. & Cheatham, T. E. 3rd PTRAJ and CPPTRAJ: software for processing and analysis of molecular dynamics trajectory data. *J. Chem. Theory Comput.* **9**, 3084–3095 (2013).

56. Hunter, J. D. Matplotlib: a 2D graphics environment. *Comput. Sci. Eng.* **9**, 90–95 (2007).

57. Case, D. A. et al. AMBER 2018. University of California, San Francisco (2018).

58. Wang, J., Wolf, R. M., Caldwell, J. W., Kollman, P. A. & Case, D. A. Development and testing of a general amber force field. *J. Comput. Chem.* **25**, 1157–1174 (2004).

59. Jorgensen, W. L., Chandrasekhar, J., Madura, J. D., Impey, R. W. & Klein, M. L. Comparison of simple potential functions for simulating liquid water. *J. Chem. Phys.* **79**, 926–935 (1983).

60. Frisch, M. J. et al. Gaussian, Inc., Gaussian 16. Revision C.01, Wallingford CT (2016).

61. Bayly, C. I., Cieplak, P., Cornell, W. & Kollman, P. A. A well-behaved electrostatic potential based method using charge restraints for deriving atomic charges: the RESP model. *J. Phys. Chem.* **97**, 10269–10280 (1993).

Acknowledgements

Author contributions

X.X. and X.L. performed protein expression, purification, crystallization, structure determination, and refinement. J.S., A.S., and L.M. performed the design, chemical synthesis, and analytical characterization of compounds. J.K. and A.J.V. performed and analyzed MD simulations supervised by R.O.D. M.J.C. and D.M. characterized the pharmacology properties of βARs and mutants supervised by R.K.S. and H.H. and P.G. X.X. performed the mutagenesis studies and radioligand binding of βAR mutants supervised by X.L. and B.K.K. K.H. performed automatic data collection and processing. The manuscript was written by X.L., R.K.S., and B.K.K., with input and suggestions from X.X., H.H., J.K., and P.G. All authors contributed to the editing of the manuscript. R.K.S., P.G., and B.K.K. initiated the project, coordinated the experiments, and supervised the overall research.

Competing interests

B.K.K. is a co-founder of and consultant for ConfometRx, Inc. The remaining authors declare no competing interests.

Additional information

Supplementary information The online version contains supplementary material available at https://doi.org/10.1038/s41467-023-37808-y.

Correspondence and requests for materials should be addressed to Brian K. Kobilka, Roger K. Sunahara, Xiangyu Liu or Peter Gmeiner.

Peer review information *Nature Communications* thanks the anonymous reviewer(s) for their contribution to the peer review of this work.

Reprints and permissions information is available at http://www.nature.com/reprints

Publisher's note Springer Nature remains neutral with regard to jurisdictional claims in published maps and institutional affiliations.

[1]State Key laboratory of Membrane Biology, Tsinghua-Peking Center for Life Sciences, School of Pharmaceutical Sciences, Tsinghua University, Beijing 100084, China. [2]Beijing Frontier Research Center for Biological Structure, Beijing Advanced Innovation Center for Structural Biology, Tsinghua University, Beijing 100084, China. [3]Department of Chemistry and Pharmacy, Medicinal Chemistry, Friedrich-Alexander University Erlangen-Nurnberg, Nikolaus-Fiebiger-Straße 10, 91058 Erlangen, Germany. [4]Department of Pharmacology, University of California San Diego School of Medicine, 9500 Gilman Drive, La Jolla, California 92093, USA. [5]Advanced Photon Technology Division, Research Infrastructure Group, SR Life Science Instrumentation Unit, RIKEN/SPring-8 Center, 1-1-1 Kouto Sayo-cho Sayo-gun, Hyogo 679-5148, Japan. [6]Precursory Research for Embryonic Science and Technology (PRESTO), Japan Science and Technology Agency, 4-1-8 Honcho, Kawaguchi, Saitama 332-0012, Japan. [7]Department of Computer Science, Stanford University, Stanford, CA 94305, USA. [8]Department of Molecular and Cellular Physiology, Stanford University School of Medicine, Stanford, CA 94305, USA. [9]Department of Structural Biology, Stanford University School of Medicine, Stanford, CA 94305, USA. [10]Institute for Computational and Mathematical Engineering, Stanford University, Stanford, CA 94305, USA. [11]Beijing Key Laboratory of Cardiovascular Receptors Research, Peking University, Beijing, China. ✉e-mail: kobilka@stanford.edu; rsunahara@health.ucsd.edu; liu_xy@mail.tsinghua.edu.cn; peter.gmeiner@fau.de